

The development and validation of the inter-wrapper flow model in sodium-cooled fast reactors

Nina Yue^{a,b}, Dalin Zhang^{a,*}, Jing Chen^a, Ping Song^a, Xin'an Wang^a, Shibao Wang^a, Suizheng Qiu^a, G.H. Su^a, Yapei Zhang^a

^a State Key Laboratory of Multiphase Flow in Power Engineering, Shaanxi Key Lab. of Advanced Nuclear Energy and Technology, School of Nuclear Science and Technology, Xi'an Jiaotong University, Xi'an 710049, Shaanxi, PR China

^b Nuclear Power Institute of China, 328 Changshun Avenue, Chengdu 610213, China

ARTICLE INFO

Keywords:

Inter-wrapper flow
Sodium-cooled fast reactor
Code development
Sensitivity analyses

ABSTRACT

The evaluation of thermal-hydraulics of core under decay heat removal conditions is essential to the safety evaluation of a sodium-cooled fast reactor. The inter-wrapper flow (IWF) has an influence on the thermal-hydraulics of core. However, the study of the flow and heat transfer of IWF was limited. In this paper, a 2D layered IWF model was developed, and some tests were simulated to validate the IWF model, including heat removal tests SHRT-17 and SHRT-45R conducted in the experimental fast reactor EBR-II and a natural circulation test performed during the PHENIX end-of-life experiment. In order to simulate all the components of the primary system, the IWF model is coupled with the Transient Thermal-Hydraulic Analysis Code for Sodium-cooled fast reactors (THACS). In the simulation without IWF model, the predicted peak temperature of the instrumented subassembly XX10 in EBR-II is about 150 K lower than test data, and the predicted average outlet temperature of reactor core in PHENIX is about 20 K higher than test data. While the predictions of THACS with IWF model agree well with the test data. The results show that the IWF can be accurately simulated by the IWF model, and the IWF model improves the accuracy of the simulations of the reactor core. Further, some sensitivity analyses were conducted to provide better reference for the study of sodium-cooled fast reactors.

1. Introduction

The sodium-cooled fast reactor (SFR) is the most promising and mature technology for generation IV nuclear systems. The development of generation IV nuclear systems is attracting growing interest (Wang et al., 2013; Liu et al., 2016). To ensure the safety of SFR, a decay heat removal (DHR) system should work under emergency conditions. When the direct heat exchangers (DHX) of the DHR system are immersed in the hot pool, the cold coolant provided by the DHX circulates in the gap region between the subassemblies. The flow in the gaps between subassemblies is known as the inter-wrapper flow (IWF). IWF can affect the thermal-hydraulic characteristics of subassemblies via two approaches. One is the radial heat conduction between subassemblies, and the other is the convection heat transfer (Kamide et al., 1998).

Nowadays, several codes for SFR have been developed by many organizations (Sun et al., 2011). SAS4A/SASSYS-1 developed by Argonne National Laboratory (ANL) is a multi-channel safety analysis code for SFR. The subassembly duct wall is normally represented by the structure (Fanning, 2012). The heat transfer between the adjacent

subassemblies is calculated by the outer structure conduction. In the NETFLOW code developed by Hiroyasu Mochizuki (2007), the IWF is regarded as stationary sodium and modeled by several layers which are defined based on the layout of subassemblies. The SAS4A/SASSYS-1 and NETFLOW can't simulate the flow characteristic in inter-wrapper and the heat transfer coefficient is difficult to give an accurate value. AQUA developed by Kamide et al. (2002) is a numerical analysis code for IWF, in which each subassembly is modeled by a rectangular duct. This method was validated by a sodium test and a water test (Kamide et al., 2002). TRIO-U is a 3D Computation Fluid Dynamic (CFD) code developed by the French Alternative Energies and Atomic Energy Commission (CEA). In the full core calculation with TRIO-U, the inter-wrapper region between two hexagonal cans is simulated with only one mesh, and the pressure drop and heat transfer correlations are used (Tenchine et al., 2012). A 3D model coupled with a 1D model for the primary system is proposed by Parthasarathy, and the IWF is simulated with two radial cells. With this method, the simulation of PFBR transient analysis of 2 h took 45 days of CPU time on 2.67 GHz processor (Parthasarathy et al., 2012). Compared with the size of the core, the width of the gap

* Corresponding author.

E-mail address: dlzhang@mail.xjtu.edu.cn (D. Zhang).

Nomenclature			
A	Area, m^2	ρ	Density, kg/m^3
a	coefficients in equations	<i>subscripts</i>	
D	Equivalent diameter, m	<i>axial</i>	Axial direction
f	Friction coefficient	<i>CV</i>	Control volume
h	Specific enthalpy, J/kg	<i>gap</i>	The inter wrapper gap
K	Thermal Conductivity, $\text{W}/\text{m}^\circ\text{C}$	<i>i</i>	Volume i in axial direction
K_G	Coefficient of local resistance	<i>in</i>	Inner
l	Pitch of IWF layer, m	<i>j</i>	Layer j of IWF
m	Axial mass flow rate, kg/s	<i>N</i>	North
p	Pressure, Pa	<i>O</i>	Outer
S	Transverse flow area, m^2	<i>P</i>	Present control volume
S_p	Source term	<i>radial, ra</i>	Radial direction
t	Time, s	<i>S</i>	South
u	Axial velocity, m/s	<i>trapezoid</i>	Trapezoid
v	Transverse velocity, m/s	<i>superscripts</i>	
w	Transverse mass flow per unit length, $\text{kg}/\text{s}/\text{m}$	r	Transverse momentum equation
x	Radial coordinate, m	z	Axial momentum equation
z	Axial coordination, m		
<i>Greek symbols</i>			
α	Relaxation factor		

between neighboring subassemblies is so small that it is difficult to perform CFD simulations on the full core with consideration of the numerous small gaps. The CFD simulations need enormous computer storage and computing time (Sun et al., 2013). In short, the IWF cannot be promptly and accurately simulated by these existing codes.

In the past, some water tests were performed to study the inter-wrapper flow. However, the influence of heat transfer in the inter-wrapper region wasn't simulated suitably in these water tests, due to the high thermal diffusivity of the sodium. a few sodium tests were conducted (Kamide et al., 1998). Owing to limited number of subassemblies, these tests are not available to study the thermal-hydraulic characteristic of the IWF. In this study, a new IWF model is developed to simulate the flow and heat transfer in inter-wrapper gap. This model can be coupled with the system analysis code easily, and the computing speed of the coupled code is fast. To insure the accuracy of the IWF model, the decay heat removal tests in EBR-II and the natural circulation test in PHENIX are chosen to validate it.

2. Description of IWF model

During the decay heat removal condition, the damper of AHX is opened and the coolant in DHX is cooled. Part of the cooled sodium flows down into the inter wrapper through the holes at the bottom of core shroud. Other cooled sodium permeates into the inner subassemblies and inter wrapper from the top of the core (Kamide et al., 2011). The IWF is driven by the fluid density difference, and the flow paths of IWF are complex. As mentioned previously, the inter-wrapper gaps are thin and numerous. For example, there are 4431 inter-wrapper gaps with 3 mm width in the PHENIX. However, the distance across flat of hexagonal subassemblies is 116.9 mm, and the cross-sectional area of hot pool is 84 m^2 . Therefore, it is difficult to simulate IWF with a 3D CFD method due to the difficult mesh generation and iterative convergence and the slow computing speed. In order to simulate the IWF, a layered IWF model is presented in this paper. In the IWF model, the inter-wrapper gaps are divided into several layers based on the layout of subassemblies. The inter-wrapper gaps between the neighboring layers of subassemblies are considered as one layer of IWF, and the inter-wrapper gaps located in the same layer are of the same color, as shown in Fig. 1.

2.1. Fundamental assumptions and governing equations

As the flow and heat transfer in the inter-wrapper gaps are complex, some basic assumptions are made as following:

- (1) The dissipated energy is little compared with the heat transfer between subassemblies, and it is neglected.
- (2) The heat conduction between two control volumes of IWF is so small that it is ignored.
- (3) The flow in circumferential direction was ignored and the solution of IWF was simplified into a two-dimensional problem.
- (4) Sodium is incompressible and the density of sodium is only a function of temperature.

Based on above assumptions, the governing equations in this model are derived from N-S equations (Tao, 2001), as shown below.

a) Mass continuity equation is

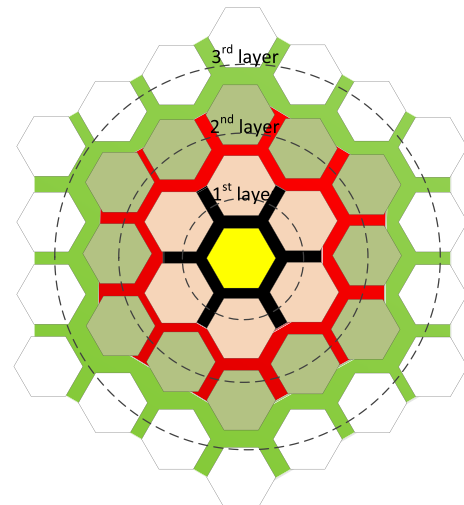


Fig. 1. Diagram of the layers of IWF.

$$A_i \frac{\partial}{\partial t} \rho_i + \frac{\partial}{\partial z} m_i + \sum_{j \in i} w_{ij} = 0. \quad (1)$$

b) Energy conservation equation is

$$A_i \frac{\partial (\rho h)_i}{\partial t} + \frac{\partial m_i h_i}{\partial z} + \sum_{j \in i} h^* w_{ij} = \bar{q}_i - \sum_{j \in i} \frac{S_{ij}}{l_{ij}} K (T_i - T_j) \quad (2)$$

where \bar{q}_i is the heat transfer from the wrapper of the adjacent sub-assemblies to volume i , W.

c) Axial momentum conservation equation is

$$\frac{\partial m_i}{\partial t} + \frac{\partial m_i u_i}{\partial z} + A_i \frac{\partial p_i}{\partial z} = -g \rho_i A_i - \sum_{j \in i} u_i^* w_{ij} - \frac{1}{2} \left(\frac{f_i}{D_i} + \frac{K_s}{\Delta z} \right) \frac{m_i^2}{A_i \rho_i} \quad (3)$$

where K_s is the local resistance coefficient.

d) Transverse momentum conservation equation is

$$\frac{\partial w_{ij}}{\partial t} + \frac{\partial (v_{ij} w_{ij})}{\partial x} = \frac{S_{ij}}{l_{ij}} (p_i - p_j) - \sum_{j \in i} m_j^* v_{ij} - \frac{1}{2} \left(\frac{f_j}{D_j} + \frac{K_G}{\Delta x} \right) \frac{|w_{ij}| w_{ij}}{S_{ij} l_{ij} \rho^*}. \quad (4)$$

where K_G is the local resistance coefficient.

In the momentum conservation equations, the pressure drops contain the frictional and local pressure drop (G.H.Su et al., 2013).

2.2. Nodalization and discretization

To avoid non-physical pressure oscillation caused by the numerical method, a staggered grid system is used for the discretization of the computational domain and conservation equations (Issa, 1983). In this staggered grid system, there are three kinds of control volumes: mass control volume, axial momentum control volume, and radial momentum control volume. Most variables except the velocities are located at the center of the mass control volume. And the axial and radial velocities are defined at the center of the axial and radial momentum control volumes, respectively. The spatial discretization is shown in Fig. 2.

Some geometric parameters, including the axial flow area, radial flow area, the control volume and the heat transfer surface area, are difficult to calculate owing to the irregular geometry, but they are essential for the simulation of the IWF. These parameters can affect the precision and convergence of numerical simulation greatly.

The subassemblies are arranged in a hexagonal array. The number of subassemblies in one layer can be expressed as

$$N = \begin{cases} 1 & j = 1 \\ 6(j-1) & j \geq 2 \end{cases} \quad (5)$$

In order to calculate the axial flow area of the IWF, the gap between the adjacent subassemblies is divided into two identical trapeziums, and the red zone in Fig. 3 is one of the trapeziums. The area of one trapezium is given by

$$A_{\text{trapezoid}} = L^2 \times \sqrt{3}/4 - 3 \times (L/2 + s/\sqrt{3})^2. \quad (6)$$

where L is the length of the side, s is the width of the gap.

The axial flow area of the layer j can be obtained by

$$A_{\text{axial}} = (36j - 12) \times A_{\text{trapezoid}}. \quad (7)$$

The transverse flow area of the layer j is equal to the sum of the transverse flow areas of the gaps in the layer j , and therefore the transverse flow area can be represented as

$$A_{\text{radial}} = 6j \times s \times d_{CV} \quad (8)$$

where d_{CV} is the length of the control volume.

The finite control volume method and the first-order upwind difference scheme and alternative direction implicit technique (ADI) are used to discretize the governing equations.

Mass continuity equation is discretized and written as

$$\rho_{j,i} A_{j,i-1/2} u_{j,i} - \rho_{j,i+1/2} A_{j,i+1/2} u_{j,i+1} + \rho_{j+1/2,i} S_{j+1,i} v_{j+1,i} - \rho_{j-1/2,i} S_{j,i} v_{j,i} = 0. \quad (9)$$

The axial momentum conservation equation is discretized and written as

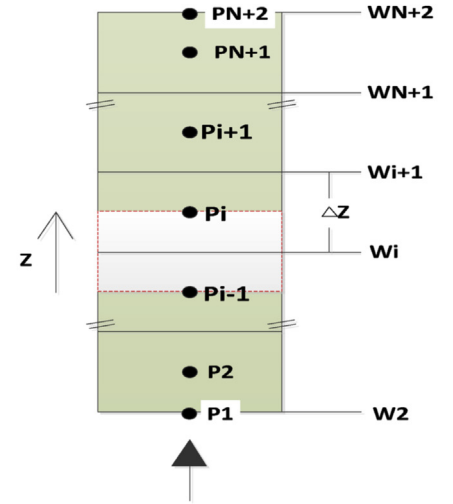
$$a_p^z u_{j,i} = a_N^z u_{j,i+1} + a_S^z u_{j,i-1} + a_O^z u_{j+1,i} + a_{IN}^z u_{j-1,i} + S_p^z, \quad (10)$$

The transverse momentum conservation equation is discretized and written as

$$a_p^r v_{j,i} = a_N^r v_{j,i+1} + a_S^r v_{j,i-1} + a_O^r v_{j+1,i} + a_{IN}^r v_{j-1,i} + S_p^r \quad (11)$$

The discretized equations are solved in a segregated way with the Semi-Implicit Method for Pressure-Linked Equations (SIMPLE) algorithm. The calculation procedures are as follows (Tao, 2001):

- 1) Read in the velocity field v^0 , u^0 and pressure field p^0 of last iterative time.
- 2) Read in the boundary condition of IWF including the inlet pressure, the inlet enthalpy and the outlet pressure.



(a) Nodalization in axial direction

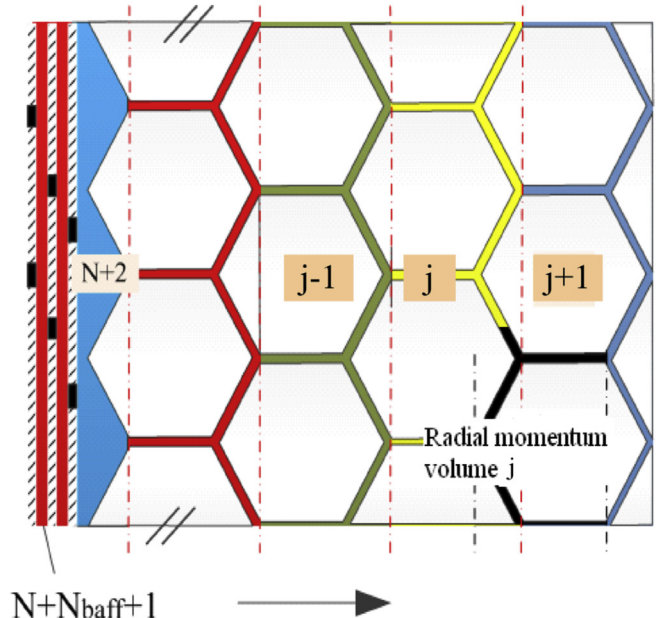


Fig. 2. The diagram of nodalization of IWF.

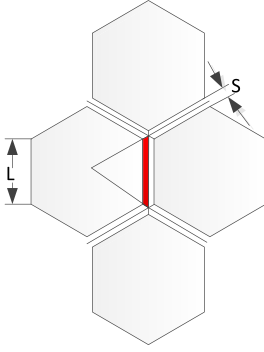


Fig. 3. The flow area exploded view.

- 3) Solve the momentum conservation equation with the pressure, velocity of previous iteration and the updated boundary condition to get the new velocity field v^* , u^* .
- 4) Solve the pressure correction equation to obtain p' .
- 5) Based on pressure correction compute the velocity correction v' , u' , and then modify the velocity field.
- 6) Update the material properties and the sources with the modified velocity and pressure field. Repeat steps 3–4 until convergence.
- 7) Repeat steps 1–6 to calculate the next iterative time.

The velocity field v^* , u^* and modified velocity field $v^* + v'$, $u^* + u'$ satisfy the momentum conservations,

$$a_p^z u_{j,i}^* = a_N^z u_{j,i+1}^* + a_S^z u_{j,i-1}^* + a_O^z u_{j+1,i}^* + a_{IN}^z u_{j-1,i}^* + b_p^z + A_{j,i} (p_{j,i-1}^* - p_{j,i}^*) \quad (12)$$

and

$$\begin{aligned} a_p^z (u'_{j,i} + u_{j,i}^*) &= a_N^z (u'_{j,i+1} + u_{j,i+1}^*) + a_S^z (u'_{j,i-1} + u_{j,i-1}^*) \\ &+ a_O^z (u'_{j+1,i} + u_{j+1,i}^*) + a_{IN}^z (u'_{j-1,i} + u_{j-1,i}^*) + b_p^z \\ &+ A_{j,i} \left((p'_{j,i-1} + p_{j,i-1}^*) - (p_{j,i}^* + p'_{j,i}) \right). \end{aligned} \quad (13)$$

Substituting Equation (14) in Equation (15) yields the following equation

$$a_p^z u'_{j,i} = \sum a_{nb} u'_{nb} + b_p^z + A_{j,i} (p'_{j,i-1} - p'_{j,i}). \quad (14)$$

Since pressure correction is the main influence factor on the velocity correction, other factors are ignored. Equation (14) is simplified into

$$a_p^z u'_{j,i} = A_{j,i} (p'_{j,i-1} - p'_{j,i}), \quad (15)$$

In the same way, $v'_{j,i}$ can be expressed as

$$d_p v'_{j,i} = S_{j,i} (p'_{j,i} - p'_{j-1,i}). \quad (16)$$

Mass continuity equation described with modified velocity field is as follows,

$$\begin{aligned} \rho_{j,i} A_{j,i-1/2} (u_{j,i}^* + u'_{j,i}) - \rho_{j,i+1/2} A_{j,i+1/2} (u_{j,i+1}^* + u'_{j,i+1}) \\ + \rho_{j+1/2,i} S_{j+1,i} (v_{j+1,i}^* + v'_{j+1,i}) - \rho_{j-1/2,i} S_{j,i} (v_{j,i}^* + v'_{j,i}) = 0. \end{aligned} \quad (17)$$

Substituting Equations (15) and (16) into Equation (17), we obtain

$$B_p p'_{j,i} = B_s p'_{j,i-1} + B_n p'_{j,i+1} + B_o p'_{j+1,i} + B_{in} p'_{j-1,i} + S_p \quad (18)$$

Convergence difficulties are often encountered in the simulation of the natural circulation. Thus some relaxation factors are introduced. With the pressure relaxation factor, the modified pressure can be expressed as

$$p = \alpha_p p' + p^*. \quad (19)$$

With the velocity relaxation factors, the momentum conservation equations can be written as follows,

$$\frac{a_p^z}{\alpha_{axial}} u_{j,i} = \sum a_{nb} u_{nb} + b_p^z + (1 - \alpha_{axial}) \frac{a_p^{z,0}}{\alpha_{axial}} u_{j,i}^0 \quad (20)$$

$$\frac{a_p^r}{\alpha_{ra}} v_{j,i} = \sum a_{nb} v_{nb} + b_p^r + (1 - \alpha_{ra}) \frac{a_p^{r,0}}{\alpha_{ra}} v_{j,i}^0, \quad (21)$$

where α_{ra} and α_{axial} are the velocity under-relaxation factors in radial and axial direction, respectively.

There are two solution methods for IWF energy. One is that the coefficient matrix of energy equation is derived and solved with iterative method, and the other one is that the enthalpy time derivatives are derived and calculated with Gear method (Yue et al., 2015). The high-thermal conductivity of sodium and the small heat capacity of IWF may result in over predicting the value of the enthalpy correction. Gear method can improve the calculation stability.

The energy conservation equation is

$$\begin{aligned} \frac{dh_{j,i}}{dt} &= [I - F_N, 0] \times h_{j,i+1} - [I F_N, 0] \times h_{j,i} + [I F_S, 0] \times h_{j,i-1} \\ &- [I - F_S, 0] \times h_{j,i} - [I - F_O, 0] \times h_{j,i} + [I F_O, 0] \times h_{j+1,i} \\ &+ [I - F_{IN}, 0] \times h_{j-1,i} - [I F_{IN}, 0] \times h_{j,i} + Q_{j,i} \end{aligned} \quad (22)$$

where $Q_{j,i}$ is the heat transfer between subassemblies and IWF.

2.3. Coupling of IWF model with THACS

2.3.1. Description of THACS code

The 1D system analysis code THACS (Transient Thermal-Hydraulic Code for Analysis of Sodium-Cooled Fast Reactor) has been developed by Xi'an Jiaotong University (Ma et al., 2015). The code can calculate single-phase and two-phase flows of sodium. One-dimensional flow with non-compressibility is assumed in the single-phase flows of sodium. For the two-phase calculation, the multi-bubble model is used in the core module for sodium. A compressible water model is applied in the water side of steam generators. THACS uses an oriented-object structure permitting the representation of any kind of hydraulic circuit, from the analytical experimental facilities to the whole reactor power plant. The code capabilities are listed as below:

- Multiple channel core thermal-hydraulic analysis;
- Point kinetic resolution including decay heat and reactivity feedback models including fuel Doppler, fuel and coolant density variations, core radial expansion, control-rod driveline expansion and coolant voiding;
- Models of metallic fuel and MOX fuel thermo-physical properties;
- Primary and intermediate loops of reactor coolant systems models, such as pipes, intermediate heat exchangers, centrifugal pumps, hot pools and cold pools, pipe-nets, air-dump heat exchangers, steam generators, inter-wrapper flow and reactor vessel auxiliary cooling systems (RVACS).

2.3.2. Coupling method

In this paper, the IWF model and THACS code were coupled with the explicit two-way coupling method in this paper. The mass and momentum of the IWF were solved with SIMPLE method, and they were calculated in the IWF model. Since the energy of the IWF was better to be solved with Gear method, and the THACS code contains the Gear method module, so the energy of the IWF was calculated in the THACS code. The boundary conditions of the IWF model are inlet pressure, outlet pressure, and inlet and outlet temperature of IWF, which were provided by THACS code. The mass flow rates of IWF were calculated by the IWF model, which were needed in the energy calculation of IWF

with the THACS code.

The coupling relationship is shown in Fig. 4. Firstly, the flow field of IWF is calculated by the IWF model with the boundary conditions, including the velocity and temperature field distribution of last time step, and the inlet pressure at last time. Secondly, the heat transfer from wrapper to IWF is calculated with THACS code. Thirdly, the mass flow rate of IWF is treated as a mass source, and the heat transfer from wrapper to IWF is considered as a heat source of the coolant in assemblies. At last, main system parameters of next time step are calculated by THACS code.

In one time step, the multi-iterations are applied to calculate the temperature and the mass flow rate. The convergence criterion is that the ratio of the residual norm of the continuity equation to the outlet mass flow rate ϵ is less than 4.0×10^{-5} .

$$\frac{\sqrt{\sum_{\text{sum of inner point}} (S_p)^2}}{q_m} \leq \epsilon \quad (23)$$

3. Validation of IWF model

3.1. EBR-II shutdown heat removal tests

3.1.1. Description of EBR-II tests

The EBR-II is a metal fueled reactor built up by ANL in 1964 and is decommissioned in 1994 (Sumner and Wei, 2012). It is a sodium-cooled, one pool type fast reactor, operating at a thermal power of 62.5 MW, with a net electrical power output of approximately 20 MW. All major primary system components are submerged in a large volume as shown in Fig. 5. A series of experiments were performed during the end-of-life of EBR-II. Two of these tests SHRT-17 and SHRT-45R were chosen as the benchmark problem for IAEA coordinated research project (CRP), which we participated in.

SHRT-17 was a loss of primary flow with scram test. The initial power for the SHRT-17 test was 57.3 MW, and the power after scram was provided by ANL. The reactor vessel accommodates 637 hexagonal subassemblies which are segregated into three regions: central core, inner blanket and outer blanket. Besides, there were two subassemblies, XX09 and XX10 specifically designed with a variety of instrumentation. They were installed to provide measurements of temperature and flow rates during tests. The XX09 was a fueled subassembly and the XX10 was a non-fueled one (Sumner and Wei, 2012). SHRT-45R was a loss of primary flow without scram test. Prior to start the SHRT-45R operation, EBR-II operated at full power level and the system had reached an equilibrium state. The auxiliary electromagnetic pump (EM) in the primary system continued to receive power from its battery while the rectifier remained tripped, as would occur during a total station blackout. The core loading pattern were different slightly for the SHRT-17 and SHRT-45R tests. However, the relative location of XX10 and other subassemblies is same, which is shown in Fig. 6. XX10 is a non-fueled subassembly surrounded by driver subassemblies. The inter-wrapper-flow of EBR-II is the thimble flow. Every subassembly has a thimble and the region between thimble wall and subassembly wall is filled with sodium. The intermediate side inlet flow rate and temperature of IHX and primary pump speed were provided by ANL as boundary conditions.

3.1.2. Simulation of EBR-II

According to the major components in the benchmark model provided by ANL, the EBR-II system units numbers and nodalization by THACS are shown in Fig. 7. Based on the design core assemblies, the core could be represented by 6 different channels. First channel is the average channel to calculate the average value of the drive core. Besides, there also are XX09, XX10, reflector 1, reflector 2 and blanket channel. The power was calculated with the point kinetics model. Three pipes have been used to simulate Z-pipe and every pipe is divided into

several volumes. IHX is simulated with a tube model. The primary side, intermediate side and the tubes wall is divided into 50 vol in axial direction respectively. The inlet pipes and inlet plena are simulated with Pipe-Net model. In the simulation, the drivers and high flow drivers are all considered as average channel, so the simulation model of IWF for XX10 was simulated as Fig. 8. One layer IWF model was used and the outer subassemblies are average channel and the inner subassembly is XX10 and is divided into 20 control volumes in axial direction.

3.1.3. Results and analyses

The simulated results of XX10 in SHRT-45R and SHRT-17 are shown in Fig. 9 and Fig. 10 respectively. It can be seen that, the calculated peak temperatures without IWF model are about 150 K lower than experiment data (Yue et al., 2015). However, the simulated data with IWF model are in good agreement with test data. It is because that XX10 is a non-fuel subassembly and its power was much lower than drive ones. Therefore, the temperature of XX10 is much lower than that of surrounding subassemblies when the heat transfer between them is ignored. However, the inter-wrapper sodium and wrappers are of high-thermal conductivity which is considered in IWF model. Thus, it is the heat transfer through IWF and wrappers that raise the temperatures of XX10.

The predicted mass flow rate of XX10 is shown in Fig. 11. As the figure shows, reversal flow appears when it is simulated without IWF. It is because the underestimated temperature of XX10 leads to the insufficient buoyancy for natural circulation. When IWF is simulated, the temperature of XX10 is much higher. Hence the reversal flow disappears and the simulation results are in good agreement with the test data.

3.2. The PHENIX natural circulation test

3.2.1. Description of PHENIX test

The PHENIX is a pool-type sodium-cooled fast reactor, built up by France in 1973 and was stopped in 1994, and it was operated at a reduced power of 350 MW(th) from 1993. Natural circulation test was carried out before the definitive shutdown of PHENIX in the year 2009. In a Coordinated Research Project (CRP) established by IAEA, several participants from seven member states addressed this transient (IAEA-TECDOC, 2013).

At first, the reactor operated in a steady-state power of 120 MW(th), with four IHXs, three primary pumps and two secondary pumps. At the beginning of the test two steam generators were dry out, which led to the increase of the reactor temperatures. Due to the feedback reactivity mechanism the power decreased slowly. At 458s, the reactor scrambled and the two secondary pumps speed decreased to 110 rpm in about 1 min. Then at 8 s after the scram the three primary pumps trip and the rotational speed automatically coasted down to 0. Then the natural circulation of the primary circuit was established (IAEA-TECDOC, 2013). The natural convection test is divided into two phases and in this

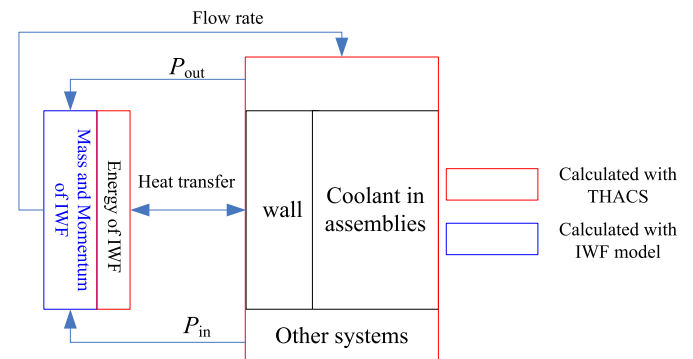


Fig. 4. Simple schematic of coupling method.

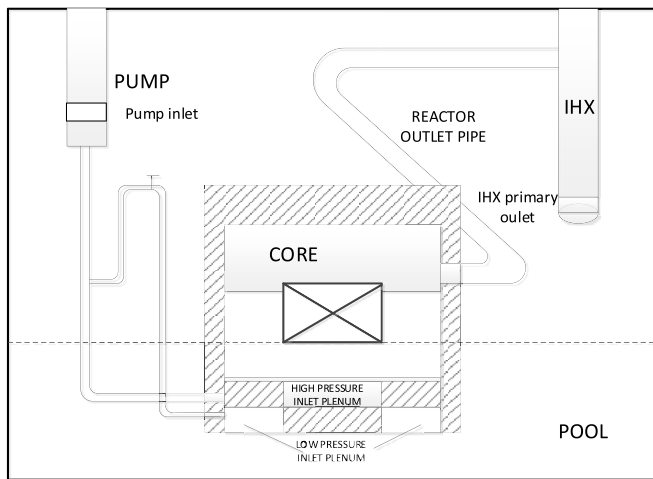


Fig. 5. Schematic of the primary system (Yue et al., 2015).

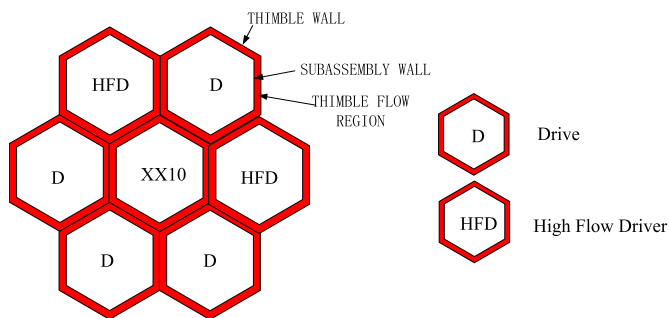


Fig. 6. The inter-wrapper flow of XX10.

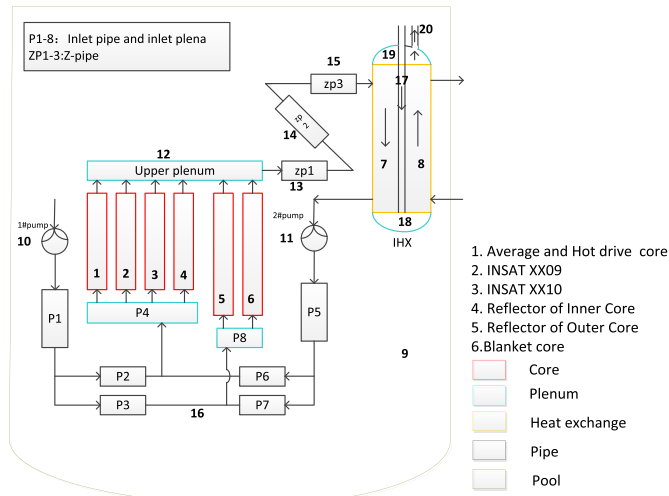


Fig. 7. Nodalization scheme for EBR-II system.

study only phase1 is simulated.

3.2.2. Simulation of PHENIX

In the simulation of this test, the boundary conditions, including the rotation speed of primary pumps, the power of core, the temperature and mass flow rate of inlet coolant in IHX secondary side, are provided in the work (IAEA-TECDOC, 2013). And the four-quadrant characteristic curves of primary pumps were also provided by CEA. The scheme of PHENIX primary system nodalization is shown in Fig. 12. In the calculation, the core is simulated with four channels, which represent the inner core, the outer core, the fertile zone and the reflector zone

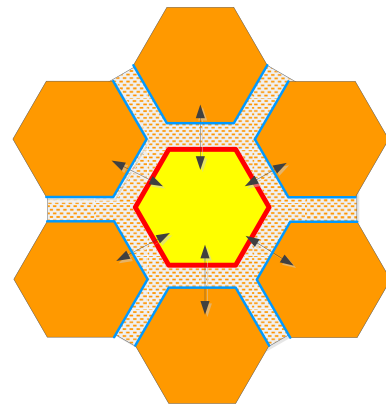


Fig. 8. The simulation model of IWF in EBR-II.

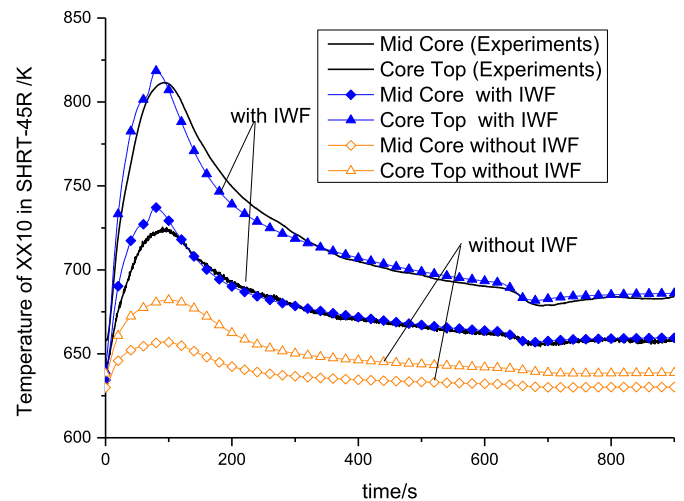


Fig. 9. The simulated temperature of XX10 in SHRT-45R (blue lines are simulated with IWF and origin lines are simulated without IWF). (For interpretation of the references to color in this figure legend, the reader is referred to the Web version of this article.)

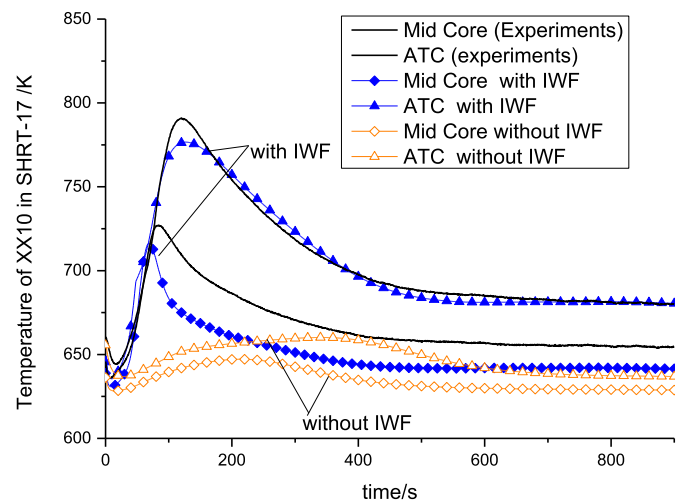


Fig. 10. The simulated temperature of XX10 in SHRT-17 (blue lines are simulated with IWF and origin lines are simulated without IWF). (For interpretation of the references to color in this figure legend, the reader is referred to the Web version of this article.)

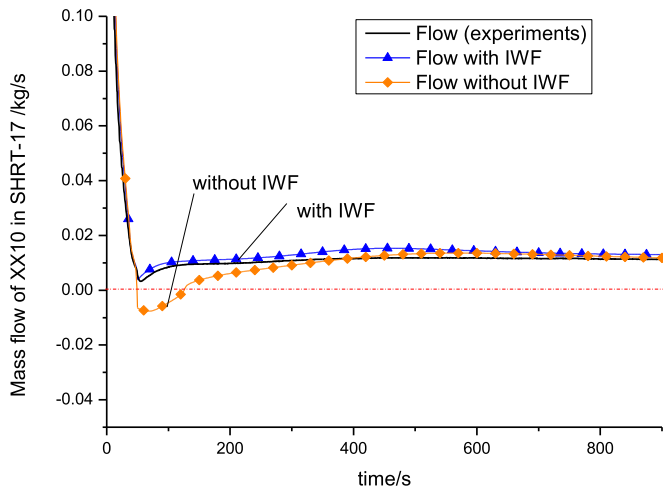


Fig. 11. The mass flow rate of XX10 in SHRT-17 (blue lines are simulated with IWF and origin lines are simulated without IWF). (For interpretation of the references to color in this figure legend, the reader is referred to the Web version of this article.)

respectively. And the subassemblies number of each channel is shown in Table 1. In addition, the IWF of PHENIX is divided into 23 layers in radial direction and 10 control volumes in axial direction. Two steady station, at 350 MW(th) and 120 MW(th) are simulated and the results are shown in Table 2. The main parameters are consistent well with the data provided by CEA.

3.2.3. Results and analyses

The transient evaluation of the inner core outlet temperature is shown in Fig. 13. As the test data shown, a 30 K temperature drop is observed at $t = 458$ s and the peak temperature (about equal to initial temperature) appear at about $t = 720$ s. It can be seen that most agencies overestimated the peak temperature. By the comparison, the prediction with IWF is in better agreement with the measured data than that without IWF. The IWF reduces the peak temperature of inner core by 20 K.

Figs. 14–16 show that the average coolant temperatures at the outlet of the outer core zone, fertile core zone and reflector zone, respectively. It is observed that, the outlet temperature of outer core and fertile zone predicted with IWF is lower than that without IWF during

Table 1

The classification of PHENIX core.

Number in code	Channel name	Number of assemblies
1	Inner core	54
2	Outer core	56
3	Fertile zone	86
4	Reflector zone	1274

Table 2

The results of steady stations of PHENIX.

Parameters	Provided by CEA	Results of THACS	error%
350 MW_{th}			
Primary flow rate in IHX/kg s ⁻¹	497.00	496.88	0.024
Core outlet temperature/K	798.15	797.66	1.2
Core flow rate/kg s ⁻¹	1988.00	1987.52	0.024
Temperature of cold pool/K	658.15	656.46	1.2
IHX primary outlet temperature/K	658.15	656.46	1.2
120 MW_{th}			
Primary flow rate in IHX/kg s ⁻¹	321.00	320.66	0.11
Core outlet temperature/K	705.15	705.67	0.79
Core flow rate/kg s ⁻¹	1284.00	1282.6	0.11
Temperature of cold pool/K	631.15	631.40	0.37
IHX primary outlet temperature/K	631.15	631.40	0.37

natural circulation phase. Conversely, the outlet temperature of reflector zone predicted with IWF is higher than that without IWF. It can be concluded that, the IWF can effectively flat the core temperature and reduce the peak temperature during natural circulation condition. The IWF is filled with sodium with high heat conduction. The heat is transferred from higher through IWF to lower temperature subassemblies. In the low flow condition, the affect is obvious. So the temperature in inner core and outer core become lower with IWF, and the temperature in reflector core become higher.

According to calculation, the total mass flow rate falls down to about 3% of initial value after the trip of primary pumps and the establishment of natural circulation. The mass flow rate of inner core and outer core is shown in Fig. 17. It can be seen that, IWF reduces the mass flow of inner core and outer core under natural circulation, while under the forced convection condition IWF has almost no effect on the mass

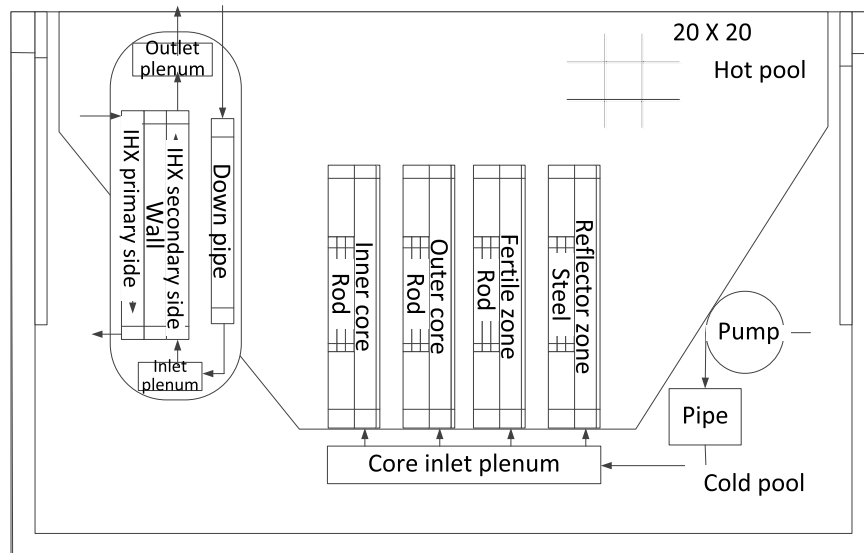


Fig. 12. Nodalization diagram of PHENIX primary loop.

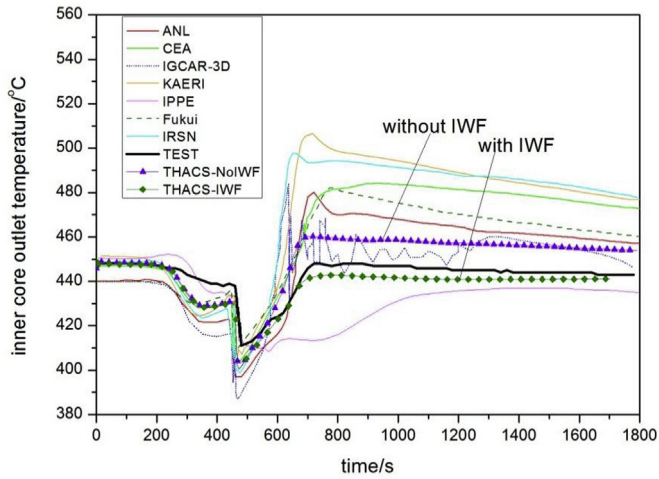


Fig. 13. Average coolant temperature at the outlet of the inner core zone (IAEA-TECDOC, 2013).

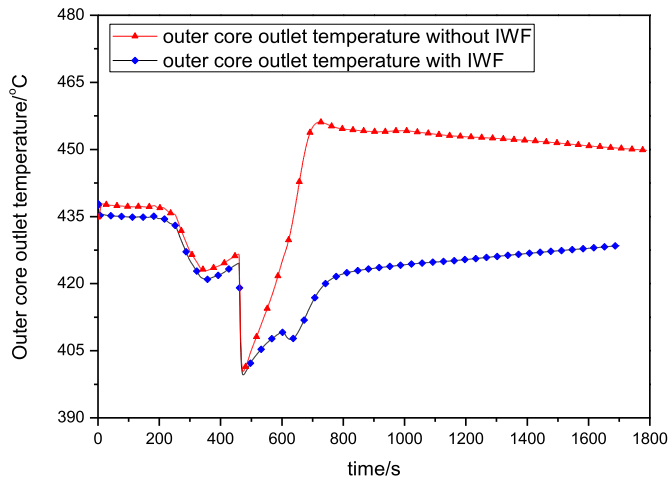


Fig. 14. Average coolant temperature at the outlet of the outer core zone.

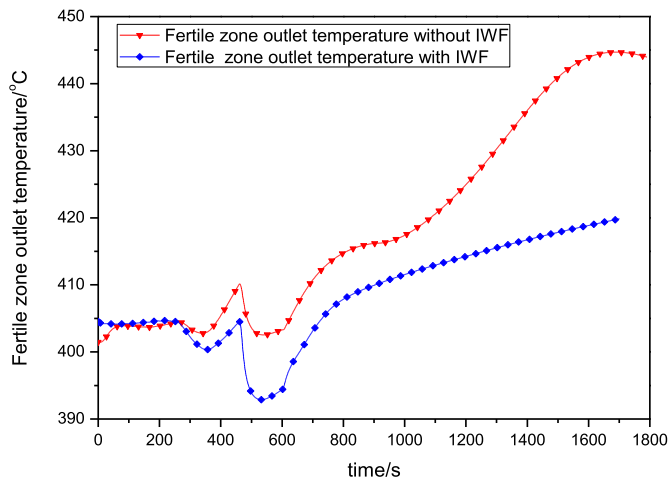


Fig. 15. Average coolant temperature at the outlet of the fertile core zone.

flow rate. Because under natural circulation condition, the flow was driven by density difference. The temperature in inner core and outer core is reduced by IWF, so the flow rate become smaller.

Fig. 18 shows the mass flow rate of fertile core zone. As can be seen, when simulated without IWF, the coolant flows reversely during 600s-

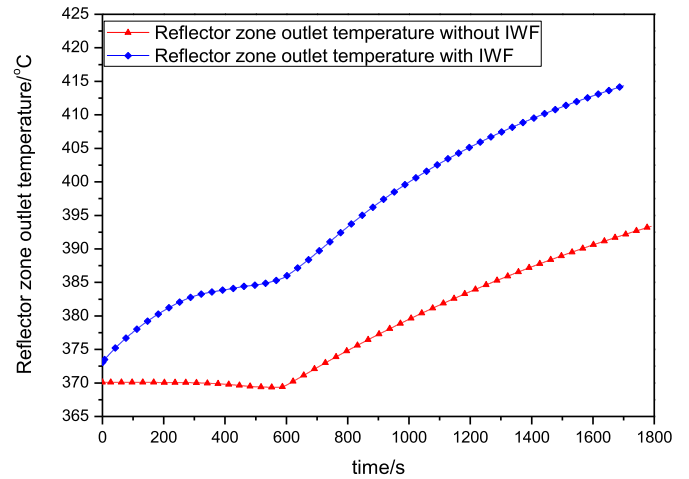


Fig. 16. Average coolant temperature at the outlet of the reflector core zone.

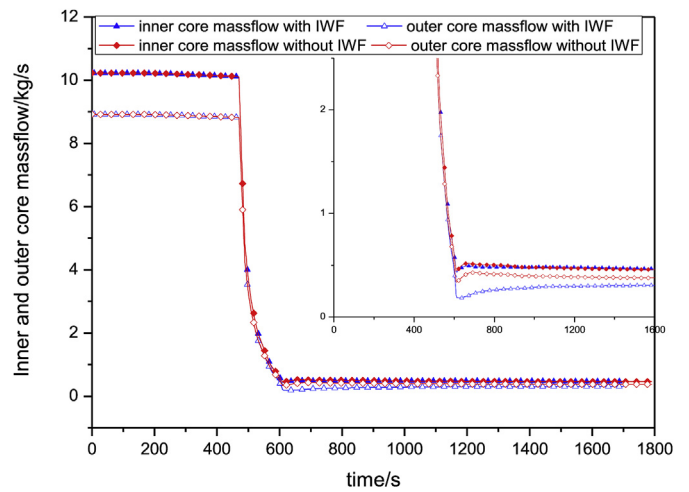


Fig. 17. Flow rate of inner core and outer core.

900s and flows upward after 900s. While simulated with IWF, the flow rate is reversed all the time after 600s. As shown in Fig. 19, the mass flow rate of the reflector zone is reversed after 600s, and the value predicted without IWF is higher than that with IWF. Therefore, IWF can reduce the ability of natural circulation between drive core and non-fuel core.

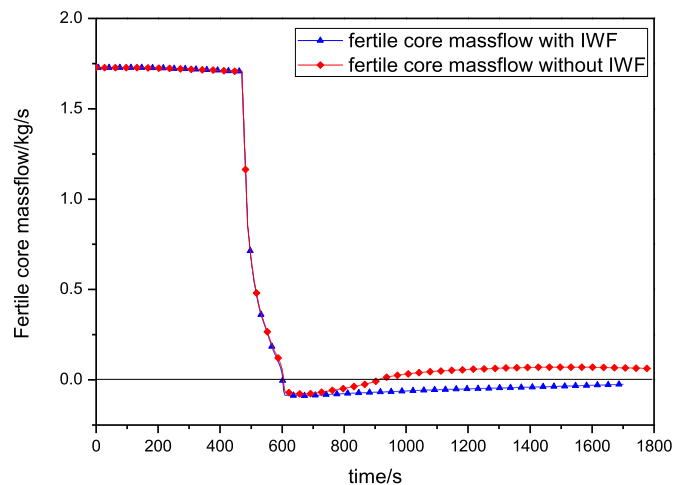


Fig. 18. Flow rate of fertile core zone.

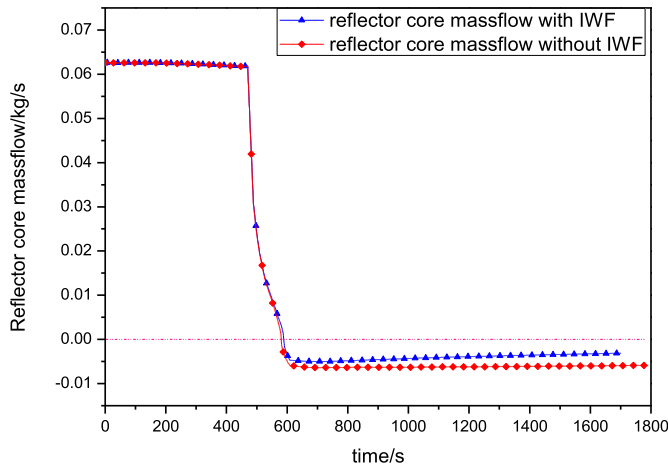


Fig. 19. Flow rate of reflector core zone.

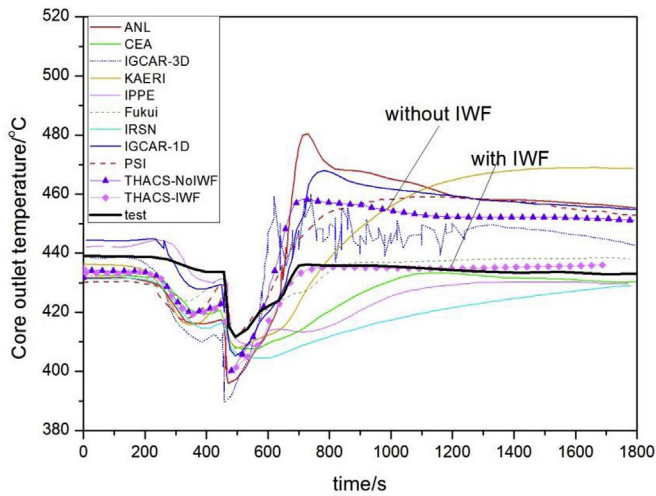


Fig. 20. Average coolant temperature at core outlet (IAEA-TECDOC, 2013).

Fig. 20 shows the average coolant temperature at core outlet. According to the test, the average outlet temperature reduced 5 K before scram owing to the reactivity feedback. Then the core scram leads to the temperature plunging 25 K. After the trip of primary pumps the average outlet temperature climbs quickly. As shown in Fig. 20, the results from 5 agencies, as well as the prediction by THACS without IWF, are much higher than the measured data (IAEA-TECDOC, 2013). Fortunately, the predictions of THACS with IWF are in very good agreement with the measured data, because the average outlet temperature determined by the upward flow channels. And the IWF reduces the outlet temperature of inner core and outer core, so the average outlet temperature dropped.

For PHENIX natural circulation test, the simulation of a 1800s transient process takes 6 h and a 24000s transient process takes 36 h and this time is relatively short. In conclusion, the 2D layer IWF model can give an accurate prediction rapidly in the transient analyses of SFR.

4. Sensitivity analyses

In this study, the sensitivity tests of influent factors on the cooling ability of IWF are carried out. The core temperature can be affected by IWF with two ways. First, the temperature of core is flattened by the IWF, which can be regarded as a conductor. Second, the subassemblies can be cooled by the IWF under natural circulation condition. Here, the heat brought out of core by the second way is called the cooling power of IWF. The cooling power and the mass flow rate of IWF can be

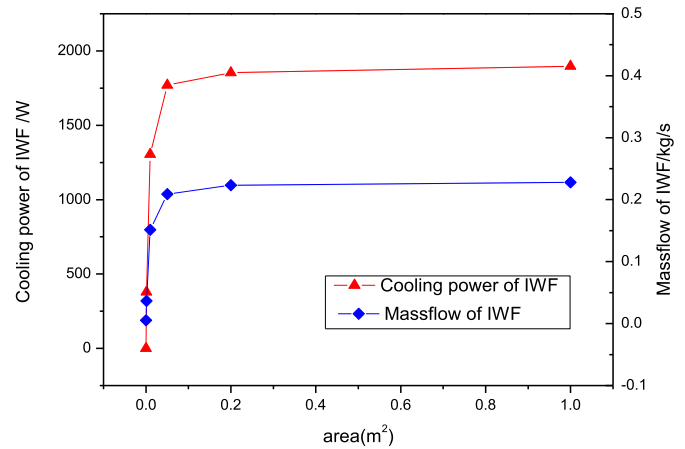


Fig. 21. The influence of inlet area on the cooling power and mass flow rate of IWF.

determined when several factors are identified, such as inlet area, width of IWF gap, resistance coefficient and flow rate of inner subassemblies.

Then, PHENIX under natural circulation condition is analyzed. There are two main parameters: the power and the total mass flow rate of core, which are 2.16 MW (th) and 57.19 kg/s, respectively. In a reference case, the inlet area at the bottom of core shroud is 0.2 m². The width of inter-wrapper gap is 3 mm. The outlet coefficient of resistance is 0.

The cooling power and flow rate of IWF are plotted against the change of inlet area in Fig. 21. It can be seen that the circulation flow rate is quite small when the inlet area is 0. The cooling power and flow rate increase rapidly with a larger area when the area varies from 0 to 0.2 m². When the area is larger than 0.2 m², the curves of cooling power and flow rate tend to be gentle. Because transverse flow area of the outermost layer of IWF (i.e., the transverse flow corresponding with the green region in Fig. 1) is about 0.2, the further increase in the inlet area has little effect on mass flow rate.

Fig. 22 shows the cooling power and flow rate data of IWF as function of width of inter-wrapper gap. It can be concluded that, the cooling power of IWF increases with an increasing in gap width. However, an increasing in gap width leads to a decrease in flow area of inner subassemblies. The gap width is determined by many factors, such as stress and deformation of wrappers.

Fig. 23 shows the cooling power and mass flow rate of IWF data as function of outlet resistance coefficient. As can be seen, the cooling power of IWF decreases with an increase in outlet resistance coefficient. In addition, the effect of the outlet resistance coefficient on cooling

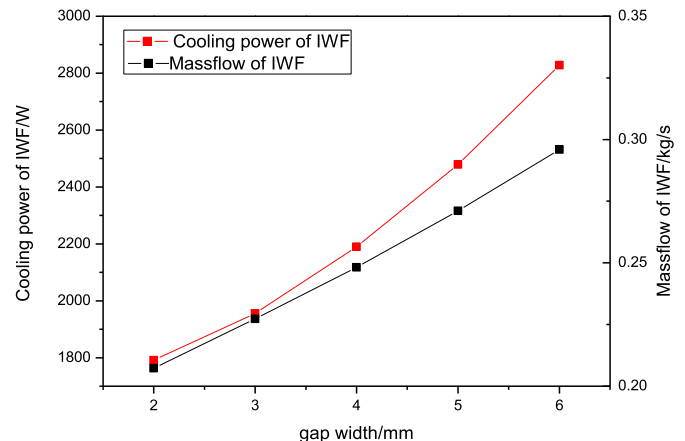


Fig. 22. The influence of gap width on the cooling power and mass flow rate of IWF.

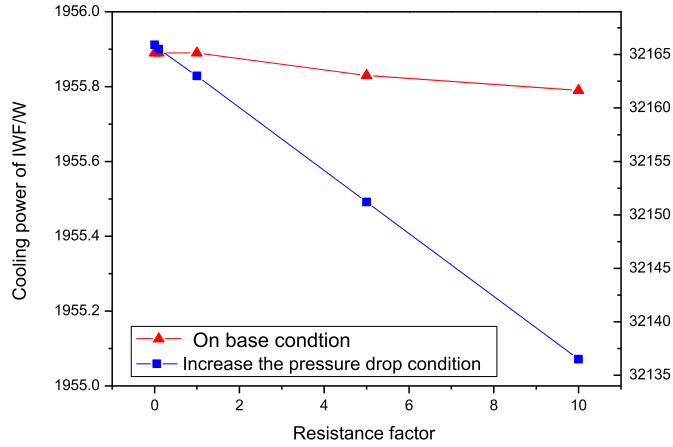


Fig. 23. The influence of export resistance factor on the cooling power and mass.

power of IWF is more obvious with a larger pressure drop between inlet and outlet. Compared with the effects of the inlet area and the gap width, the effect of the outlet resistance coefficient can be negligible. Because thin gaps and small flow rate leads to large frictional coefficient, and the frictional coefficient is far greater than outlet resistance coefficient.

The cooling power and flow rate of IWF are plotted against the change of the total mass flow rate of inner subassemblies shown in Fig. 24. It can be seen that the cooling power and mass flow rate of IWF increases with a decrease in total mass flow rate. With the decrease of the mass flow rate, the growth rate of cooling power of IWF goes up. It is because that decay heat was removed mainly by the coolant in inner subassemblies. Therefore, a decrease of mass flow rate leads to an increase of temperature in subassemblies. Then the heat transfer between subassemblies and IWF is improved, corresponding to an enhanced

Appendix

The equations (10), (11), (18) and (22) are given in detail as follows.

The axial momentum conservation equation is written as

$$a_P^z u_{j,i} = a_N^z u_{j,i+1} + a_S^z u_{j,i-1} + a_O^z u_{j+1,i} + a_{IN}^z u_{j-1,i} + S_P^z \quad (24)$$

where,

$$a_P^z = a_P^{z,0} + [|F_N, 0|] + [| - F_S, 0|] + [| - F_O, 0|] + [|F_{IN}, 0|]$$

$$a_P^{z,0} = \frac{\rho_{j,i} \frac{1}{2} \Delta V}{\Delta t}$$

$$a_N^z = [| - F_N, 0|]$$

$$a_S^z = [|F_S, 0|]$$

$$a_O^z = [|F_O, 0|]$$

$$a_{IN}^z = [| - F_{IN}, 0|]$$

$$S_P^z = A_{j,i} (p_{j,i-1} - p_{j,i}) - \frac{1}{2} \left(\frac{f_{j,i} \Delta z}{D_{j,i}} + k_{j,i} \right) \rho_{j,i} u_{j,i}^2 A_{j,i} + a_P^{z,0} u_{j,i}^0$$

and,

$$F_N = \rho_{j,i} A_{j,i} \frac{u_{j,i} + u_{j,i+1}}{2}$$

$$F_S = \rho_{j,i-1} A_{j,i-1} \frac{u_{j,i-1} + u_{j,i}}{2}$$

$$F_O = \rho_{j+1,i} v_{j+1,i} S_{j+1,i}$$

$$F_{IN} = \rho_{j-1,i} v_{j-1,i} S_{j-1,i}$$

The transverse momentum conservation equation is written as

$$a_P^r v_{j,i} = a_N^r v_{j,i+1} + a_S^r v_{j,i-1} + a_O^r v_{j+1,i} + a_{IN}^r v_{j-1,i} + S_P^r$$

natural circulation. It is obvious that the effect of core mass flow rate on cooling power of IWF is largest. Therefore, except flattening the temperature of core, the IWF not only can flat the temperature of core, but also has a strong cooling ability under low core flow rate and high temperature conditions.

5. Conclusion

A 2D IWF model, which has a quick computing speed and can be coupled with the 1D analyses code easily, was developed to simulate the flow circulation and heat transfer in inter-wrapper. Then two benchmark problems, the decay heat removal tests of EBR-II and the natural circulation test of PHENIX, were chosen to validate the IWF model. The predictions calculated by THACS with IWF model are in a better agreement with the experiment data than that calculated by THACS without IWF model. In the simulation of PHENIX natural circulation test, due to the application of IWF model, the peak temperature of the inner core can be reduced by about 20 K while that of fertile core zone can be decreased by close to 30 K. Therefore IWF plays an important role in reducing the hot-spot temperature and improving the security of reactors. Besides, some sensitivity analyses were done. The key parameters that affect the cooling power of IWF are the inlet area in the bottom of core shroud and the flow rate in inner subassemblies. Some holes with suitable sized in the bottom of core shroud can effectively improve the cooling ability of IWF. In addition, IWF has a strong cooling ability under small core flow rate conditions. In a conclusion, the IWF effects cannot be ignored in the analyses of sodium-cooled fast reactors under the decay heat removal condition.

Acknowledgement

The authors would like to thank the support from Natural Science Foundation of China (Grant Nos. 11475132) and National Natural Science Foundation of China (Grant Nos. 11605131).

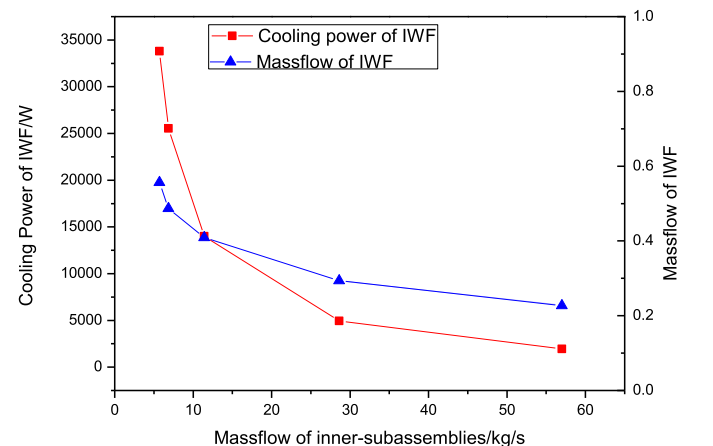


Fig. 24. The influence of the total mass flow of inner-subassemblies on the cooling power and mass flow rate of IWF.

Where,

$$\begin{aligned} a_p^r &= a_p^{r,0} + [F_N, 0] + [I - F_S, 0] + [I - F_O, 0] + [F_{IN}, 0] \\ a_p^{r,0} &= \frac{\rho_{j,i} S_{j,i} \Delta z}{\Delta t} \\ a_N^r &= [I - F_N, 0] \\ a_S^r &= [F_S, 0] \\ a_O^r &= [F_O, 0] \\ a_{IN}^r &= [I - F_{IN}, 0] \\ S_p^r &= (P_{j,i} - P_{j-1,i}) S_{j-1/2,i} - \frac{1}{2} \left(\frac{f_{j,i} l_{j,i}}{d_{j,i}} + k_G \right) \rho_{j,i} S_{j,i} v_{j,i}^2 + a_p^{r,0} v_{j,i}^0 \end{aligned}$$

and,

$$\begin{aligned} F_N &= \rho_{j,i+1/2} u_{j,i+1} A_{j,i+1} \\ F_S &= \rho_{j,i-1/2} u_{j,i} A_{j,i} \\ F_O &= \rho_{j,i} S_{j,i} \frac{v_{j+1,i} + v_{j,i}}{2} \\ F_{IN} &= \rho_{j-1,i} S_{j-1,i} \frac{v_{j-1,i} + v_{j,i}}{2} \end{aligned}$$

where, S_p^r and S_p^z are the source terms of discretization equations for w and u equations respectively.

The equation for pressure modification is

$$B_p p'_{j,i} = B_s p'_{j,i-1} + B_n p'_{j,i+1} + B_o p'_{j+1,i} + B_{in} p'_{j-1,i} + S_p \quad (26)$$

where

$$\begin{aligned} B_p &= \frac{A_{j,i} \rho_{j,i} A_{j,i-1/2}}{a_p} + \frac{\rho_{j,i+1/2} A_{j,i+1/2} A_{j,i}}{a_{p+1}} + \frac{\rho_{j+1/2,i} S_{j+1,i} S_{j+1/2,i}}{d_{p+1}} + \frac{\rho_{j-1/2,i} S_{j,i} S_{j+1/2,i}}{d_p} \\ B_s &= \frac{A_{j,i-1} \rho_{j,i} A_{j,i-1/2}}{a_p} \\ B_n &= \frac{\rho_{j,i+1/2} A_{j,i+1/2} A_{j,i+1}}{a_{p+1}} \\ B_o &= \frac{\rho_{j+1/2,i} S_{j+1,i} S_{j+3/2,i}}{d_{p+1}} \\ B_{in} &= \frac{\rho_{j-1/2,i} S_{j,i} S_{j-1/2,i}}{d_p} \\ S_p &= \rho_{j,i} A_{j,i-1/2} u_{j,i}^* - \rho_{j,i+1/2} A_{j,i+1/2} u_{j,i+1}^* + \rho_{j+1/2,i} S_{j+1,i} v_{j+1,i}^* - \rho_{j-1/2,i} S_{j,i} v_{j,i}^* \end{aligned}$$

The energy conservation equation is

$$\begin{aligned} \frac{dh_{j,i}}{dt} &= [I - F_N, 0] \times h_{j,i+1} - [F_N, 0] \times h_{j,i} + [F_S, 0] \times h_{j,i-1} \\ &\quad - [I - F_S, 0] \times h_{j,i} - [I - F_O, 0] \times h_{j,i} + [F_O, 0] \times h_{j+1,i} \\ &\quad + [I - F_{IN}, 0] \times h_{j-1,i} - [F_{IN}, 0] \times h_{j,i} + Q_{j,i} \end{aligned} \quad (27)$$

Where,

$$\begin{aligned} F_N &= \rho_{j,i+1/2} u_{j,i+1} A_{j,i+1} \\ F_S &= \rho_{j,i-1/2} u_{j,i} A_{j,i} \\ F_O &= \rho_{j+1,i} v_{j+1,i} S_{j+1,i} \\ F_{IN} &= \rho_{j-1,i} v_{j-1,i} S_{j,i} \end{aligned}$$

where $Q_{j,i}$ is the exchanged heat between subassemblies and IWF.

References

- Fanning, T., 2012. The SAS4A/SASSYS-1 Safety Analysis Code System. ANL/NE-12/4. Nuclear Engineering Division, Argonne National Laboratory.
- IAEA-TECDOC, 2013. Benchmark Analyses of the Natural Circulation Test Performed during the PHENIX End-of-life Experiments: Final Report of a Co-ordinated Research Project 2008-2011. No. 1703.
- Issa, R., 1983. Numerical methods for two- and three-dimensional recirculating flows. Computat. Meth. Turbulent Transonic and Viscous Flows 1983, 183–211.
- Kamide, H., Hayashi, K., Toda, S., 1998. An experimental study of inter-subassembly heat transfer during natural circulation decay heat removal in fast breeder reactors. Nucl. Eng. Des. 183, 97–106.

- Kamide, H., Nagasawa, K., Kimura, N., Miyakoshi, H., 2002. Evaluation method for core thermohydraulics during natural circulation in fast reactors. Numerical predictions of inter-wrapper flow. JSME Int. J. Ser. B Fluids Therm. Eng. 45, 577–585.
- Kamide, H., Kobayashi, J., Hayashi, K., 2011. Sodium experiments of buoyancy-driven penetration flow into low-power subassemblies in a sodium-cooled fast reactor during natural circulation decay heat removal. Nucl. Technol. 175, 628–640.
- Liu, L., Zhang, D., Lu, Q., et al., 2016. Preliminary neutronic and thermal-hydraulic analysis of a 2 MW thorium-based molten salt reactor with solid fuel. Prog. Nucl. Energy 86, 1–10.
- Ma, Z., Yue, N., Zheng, M., Hu, B., Su, G., Qiu, S., 2015. Basic verification of THACS for sodium-cooled fast reactor system analysis. Ann. Nucl. Energy 76, 1–11.
- Mochizuki, H., 2007. Inter-subassembly heat transfer of sodium cooled fast reactors: validation of the NETFLOW code. Nucl. Eng. Des. 237, 2040–2053.

- Parthasarathy, U., Sundararajan, T., Balaji, C., Velusamy, K., Chellapandi, P., Chetal, S., 2012. Decay heat removal in pool type fast reactor using passive systems. *Nucl. Eng. Des.* 250, 480–499.
- Su, G.H., Wenxi Tian, S.Q., et al., 2013. Thermal Hydraulic Numerical Analysis of Nuclear Power System.
- Sumner, T., Wei, T., 2012. Benchmark Specifications and Data Requirements for EBR II Shutdown Heat Removal Tests SHRT 17 and SHRT 45R. Nuclear Engineering Division Argonne National Laboratory ANL-ARC-226-(Rev 1).
- Sun, K., Krepel, J., Mikityuk, K., Pelloni, S., Chawla, R., 2011. Void reactivity decomposition for sodium-cooled fast reactor in equilibrium fuel cycle. *Ann. Nucl. Energy* 38, 1645–1657.
- Sun, K., Chenu, A., Krepel, J., Mikityuk, K., Chawla, R., 2013. Coupled 3D-neutronics/thermal-hydraulics optimization study for improving the response of a 3600 MWth SFR core to an unprotected loss-of-flow accident. *Nucl. Technol.* 183, 484–503.
- Tao, W.Q., 2001. Numerical Heat Transfer. Xi'an Jiaotong University Press, Xi'an.
- Tenchine, D., Barthel, V., Bieder, U., Ducros, F., Fauchet, G., Fournier, C., Mathieu, B., Perdu, F., Quemere, P., Vandroux, S., 2012. Status of TRIO_U code for sodium cooled fast reactors. *Nucl. Eng. Des.* 242, 307–315.
- Wang, C., Zhang, D., Qiu, S., Tian, W., Su, G., 2013. Study on the characteristics of the sodium heat pipe in passive residual heat removal system of molten salt reactor. *Nucl. Eng. Des.* 265, 691–700.
- Yue, N., Ma, Z., Cai, R., Hu, B., Su, G., Qiu, S., 2015. Thermal-hydraulic analysis of EBR-II shutdown heat removal tests SHRT-17 and SHRT-45R. *Prog. Nucl. Energy* 85, 682–693.